processes

MDPI

Article

A New Model to Predict Mudstone Failure Behavior from Brittle to Ductile Caused by Confining Pressures

Sheng Wang [1,2], Kaizhou Xu [1], Wanchun Zhao [2,3,*], Xiaofei Fu [2,3], Xuesong Lu [4] and Zhenlong Song [5]

[1] School of Physics and Electronic Engineering, Northeast Petroleum University, Daqing 163318, China; wangsheng10@126.com (S.W.); 13954790589@163.com (K.X.)
[2] Key Laboratory of Oil & Gas Reservoir and Underground Gas Storage Integrity Evaluation of Heilongjiang Province, Daqing 163318, China; fuxiaofei2008@sohu.com
[3] Institute of Unconventional Oil & Gas, Northeast Petroleum University, Daqing 163318, China
[4] Research Institute of Petroleum Exploration and Development, PetroChina, Beijing 100083, China; luxs@petrochina.com.cn
[5] College of Resources and Environmental Sciences, Chongqing University, Chongqing 400030, China; zhenlongsong@cqu.edu.cn
* Correspondence: zhaowanchun@nepu.edu.cn

Abstract: Understanding the failure behavior and mechanisms of mudstone is very important for engineering applications. While confining pressures play an important role in mudstone deformation, the limitations of laboratory conditions and mudstone sample preparation preclude scaled models of the mechanisms of deformation transition from brittle to ductile, especially for high confining pressures. In this study, dry indurated mudstone of the Kuqa depression in North China acted as the prototype rock for a numerical model. We performed numerical experiments for different confining pressures. Overall, the numerical model captured the stress–strain behavior and failure modes demonstrated by triaxial loading experiments from the laboratory at low confining pressures. Subsequently, the mudstone failure modes were predicted for high pressures. A new model to predict brittle–ductile failure behavior is proposed based on the understanding of the mudstone failure mechanism. The model showed the following. (i) For brittle failure stages, a shear dilatancy fracture is developed at low confining pressures. The rock failure modes undergo a high-angle shear fracture and a high-angle conjugate shear fracture. (ii) For brittle–ductile transition failure stages, a shear compaction fracture appears in rock deformation at high confining pressures. The fracture modes are exhibited as low-angle shear fractures and low-angle conjugate shear fractures.

Keywords: mudstone failure mechanism; brittle–ductile transition; confining pressure; numerical model

check for updates

Academic Editor: Yidong Cai

Received: 22 December 2024
Revised: 14 January 2025
Accepted: 17 January 2025
Published: 23 January 2025

Citation: Wang, S.; Xu, K.; Zhao, W.; Fu, X.; Lu, X.; Song, Z. A New Model to Predict Mudstone Failure Behavior from Brittle to Ductile Caused by Confining Pressures. *Processes* **2025**, *13*, 308. https://doi.org/10.3390/pr13020308

1. Introduction

The mechanical properties of rock have been a focus of several research studies such as hydraulic fracturing and wellbore stability analysis [1,2]. The confining pressure can significantly affect the mechanical failure behavior of rock [3]. With increases in the confining pressure, rock's ductility increases [4,5] and the yield limit decreases [6]. Therefore, the confining pressure is often considered in rock mechanics experiments [7]. However, rock brittle failure or brittle–ductile transition failure primarily involves cataclastic deformation mechanisms, which are sensitively dependent on pressure but relatively insensitive to temperature [8,9]; this is also described as "low-temperature brittle–ductile transition" [10]. It should be noted that thermally activated deformation mechanisms dominate in crystal plasticity and diffusion mass transfer, resulting in plastic flow, which is not within the scope of this research. A large number of studies show that increases in the confining pressure inhibit tensile fracture propagation and weaken the brittleness of rock [11,12].

Rock deformation has three stages: brittle, brittle–ductile transition, and ductile [13–15]. Deformation mechanisms can be divided into brittle cracking, brittle–plastic transition, and plastic deformation mechanisms. In the brittle stage, the deformation mechanism of microcracks and frictional sliding between particles, which are related to macroscopic fracture, is usually dominated by fracture. However, in the ductile region, the complex interaction of various deformation mechanisms may cause the elastic deformation of amorphous plasticity, diffusion mass transfer, and fragmentation [16].

In experimental rock deformation, from the stress–strain behavior, the main distinction between brittle and ductile behavior is the ability to undergo substantial permanent strain without macroscopic fracture [16]. The brittle stage is dominated by shear rupture and microcracks, which are mainly developed by axial splitting or shear fracture with a peak strain of less than 3% [17]. There is then a strain-softening process with a rapid stress drop after the peak stress [13,18,19]. The brittle–ductile stage develops local failure, forming conjugate shear fracture or complex fracture [20]. In this stage, the peak strain is generally between 3% and 5%, with a gradual stress drop [18,21]. Both the brittle and brittle–ductile deformation phases have an acoustic emission response [20,22]. In the ductile deformation stage, the peak strain is generally greater than 5% [21] and cataclastic or ductile flow occurs [23].

Under low confining pressures, the internal friction angle and cohesion of rocks are generally considered to be constant. Rock failure mechanisms and modes can be described well by the Mohr–Coulomb failure criterion [24–26]. When rock failure modes transition from brittle to ductile, the cohesion and friction angle vary with the increase in the confining pressure. In this situation, the Mohr failure envelope is generally a quadratic curve [3,27], which is not suitable for the linear Mohr–Coulomb failure criterion. For deep layers, the rock generally undergoes ductile failure with greater cumulative strain. Due to the limitations of experimental instruments, it is difficult to assess rock deformation styles under larger strain ranges, although Iyare et al. [13] recently observed mudstone failure behavior at a confining pressure of up to 130 MPa in a triaxial loading experiment. Therefore, the question now is the following: How can deformation mechanisms and deformation styles at high confining pressures be described?

In this study, a combination of laboratory experiments and numerical modeling was used to simulate mechanical deformation evolution modes with increasing confining pressures. For the outcrop mudstone in the Kuqa depression, four intact mudstone samples were successfully drilled, and the average mechanical parameters of rock under low temperature and pressure were obtained by a conventional triaxial loading experiment. The numerical code FLAC3D was used for the modeling performed in this study. Cylindrical numerical models were constructed, and the same loading conditions as the physical experiment were applied to carry out the numerical experiment. Adjusting the numerical model grid numbers and loading rates in the numerical experiments allowed the numerical model to capture the stress–strain behavior and failure modes demonstrated by the laboratory experiments at discrete confining pressure intervals, and the numerical model was calibrated. On the basis of the calibrated numerical model, the failure behavior of mudstone under high pressure was predicted. A failure mechanism caused by confining pressures was explored, which explained the experimental simulation results well. As a result, a new model to predict brittle–ductile failure behavior with confining pressures is proposed.

2. Rock Physical–Mechanical Property Test in the Laboratory

2.1. Rock Sample Description and Preparation

The experimental samples consist of Jidike (N1j) mudstone, sourced from the outcrop of Dongqiu anticline in the Kuqa Depression. The Kuqa Depression is located in the northern region of the Tarim Basin in China, with geographical coordinates of 41°43′05.97″ N, 82°57′48.47″ E. The strike direction is NEE, and the basin extends approximately 300 km in length along the EW direction, 30–80 km in width along the NS direction, and covers an area of about 2.8×10^4 km^2 [28] (Figure 1). The region is part of the foreland depression at the south foot of the Tianshan fold belt and is a key area for natural gas exploration in the Tarim basin at present. It is rich in natural gas resources, which could serve as a significant source for the West-to-East Gas Transmission Project in China.

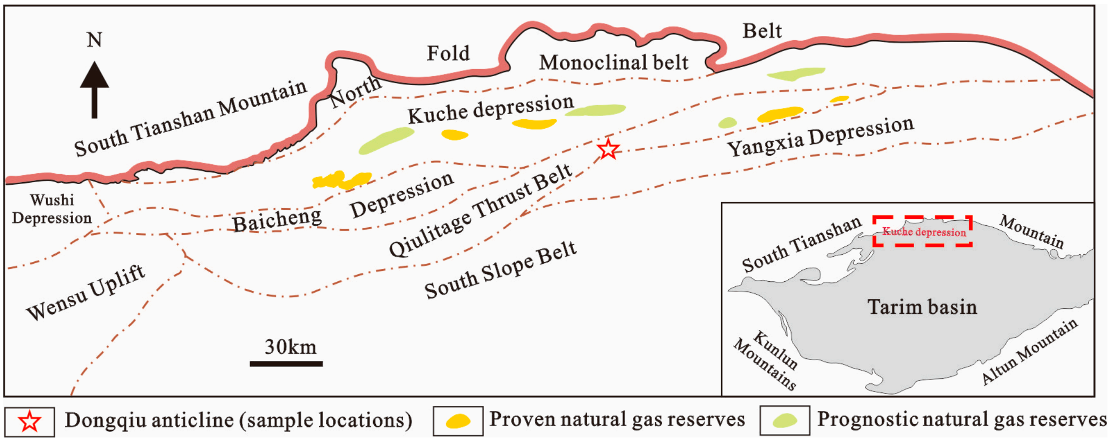

Figure 1. Simplified structure distribution map of the Kuqa Depression in the Tarim basin and the location of the sampled area on the outcrop (modified according to Wang et al. [15]).

The mudstone is highly indurated and has experienced multiple episodes of uplift and burial, with the maximum burial depth reaching about 1700 m [5]. The outcrop sample is relatively fresh after deep excavation with an excavator, showing no large-scale weathering, maintaining good stratification and lacking natural fracture. To meet the requirements for rock mechanics testing, a mudstone sample with flat layer, large-scale block and no fracture was selected for centralized sampling, ensuring that the lithology and heterogeneity of the sample have minimal impact on the rock's mechanical properties. The height–aspect ratio of the sample is usually kept at 2:1 to avoid the end-effect problem described by Paterson and Wong [16]. In this experiment, four standard cylindrical samples, each with a diameter of about 25 mm and a height of approximately 50 mm, were prepared by drilling, cutting and grinding natural cores. To prevent damage to the samples before the loading test, a sound velocity test is conducted first. The non-uniformity error at both ends of each sample is kept below 0.5 mm, the error in height and diameter is less than 0.3 mm, and the maximum deviation of the end face perpendicular to the sample axis is less than 0.25° [15]. For cylindrical samples, the two ends are typically made parallel and free from inclination by sanding or using a grinding machine. Precision measuring tools or optical instruments can be used to ensure that the center of each sample aligns with the center of the axial loading base.

2.2. Experimental Methods

Crystals of different minerals have specific X-ray diffraction (XRD) patterns. For each mineral, the peak intensity of the characteristic X-rays in the pattern is directly proportional to the abundance of the mineral, allowing the mineral composition of the sample to be determined using the D/max–2200–X-ray diffractometer produced by Bruker Corporation in Rheinstetten, Germany [29,30]. Before the experiment, the sample was ground and screened with mortar. We selected the powder sample with particle size larger than 200 mesh, weighing about 2.00–3.00 g. The specimens were then dried at 60 °C in an oven for at least 12 h and allowed to cool to room temperature. The experimental conditions were as follows: voltage 40 kV, current 200 mA, using Cu target Kα rays (λ = 0.154056 nm) and scanning angle range (2θ) 5°~80° with step length of 0.01°.

To obtain the strain–strain curve and failure behavior of mudstone under different confining pressure, the experiments were conducted using the TAW–2000 microcomputer controlled electro-hydraulic servo rock triaxial testing machine ($\sigma_1 > \sigma_2 = \sigma_3$) produced by Changchun City Chaoyang Test Instrument Co., Ltd., Changchun, China (Figure 2). The maximum axial pressure of the testing was 2000 kN. The confining pressure control system has an upper limit of 200 MPa. The load cell is located outside the vessel and measures the load on the upper piston of the sample assembly. The specimens are placed in a PVC jacket to isolate them from the confining fluid. During the triaxial compression test, the confining pressure should be increased to a predetermined value at a rate of 0.05 MPa/s to meet the experimental requirements, and then the axial pressure was applied at a rate of 0.005 m/s until the rock failed. All data, including the stress–strain curve and mechanical parameters, were measured and recorded automatically by the control program.

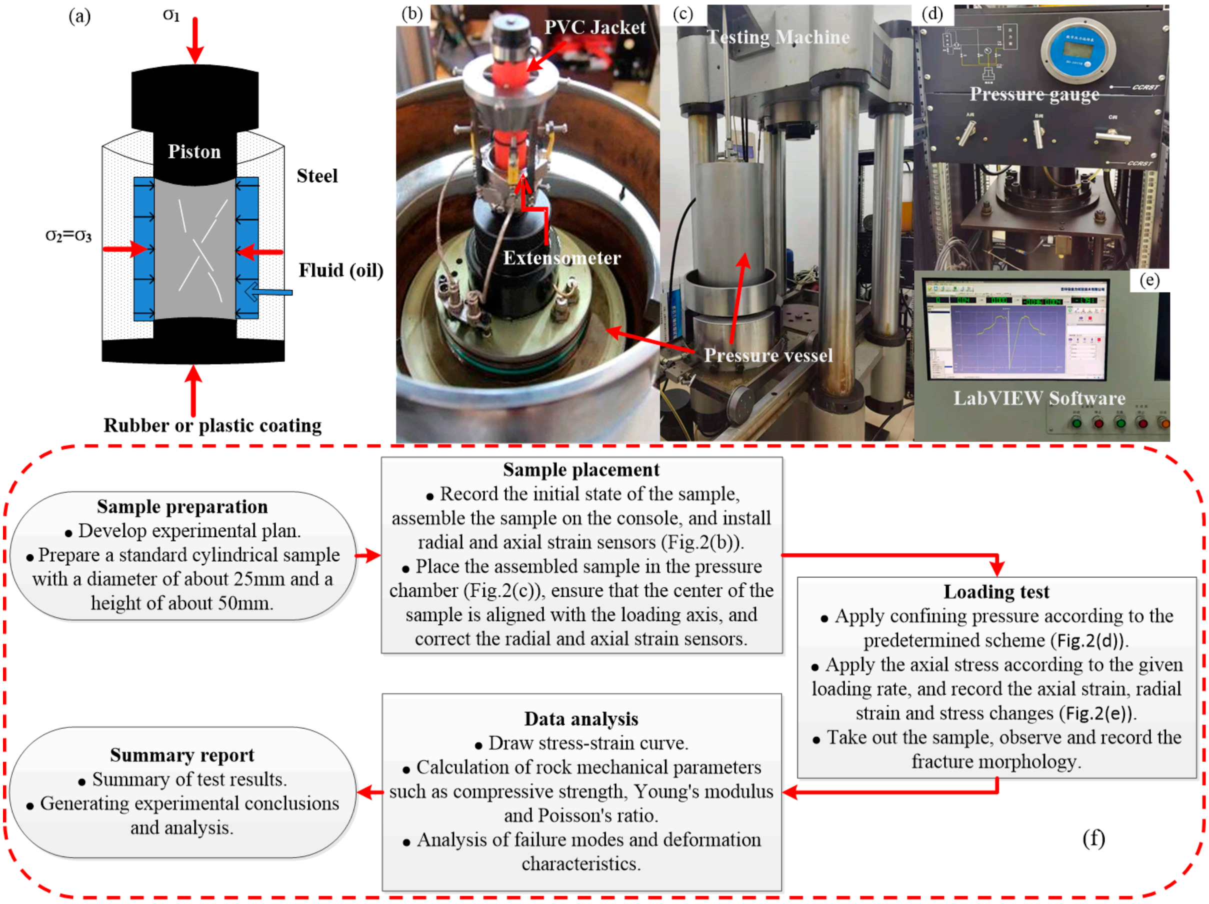

Sample preparation
- Develop experimental plan.
- Prepare a standard cylindrical sample with a diameter of about 25mm and a height of about 50mm.

Sample placement
- Record the initial state of the sample, assemble the sample on the console, and install radial and axial strain sensors (Fig.2(b)).
- Place the assembled sample in the pressure chamber (Fig.2(c)), ensure that the center of the sample is aligned with the loading axis, and correct the radial and axial strain sensors.

Loading test
- Apply confining pressure according to the predetermined scheme (Fig.2(d)).
- Apply the axial stress according to the given loading rate, and record the axial strain, radial strain and stress changes (Fig.2(e)).
- Take out the sample, observe and record the fracture morphology.

Data analysis
- Draw stress-strain curve.
- Calculation of rock mechanical parameters such as compressive strength, Young's modulus and Poisson's ratio.
- Analysis of failure modes and deformation characteristics.

Summary report
- Summary of test results.
- Generating experimental conclusions and analysis.

Figure 2. Schematic of triaxial compression test process (**a**); specimen assembly, placed inside the pressure vessel (**b**); outside view of the triaxial apparatus (**c**); loading confining pressure device (**d**); LabVIEW software (2012), which records all data in real time using (**e**); test process and method flow chart (**f**).

In this study, we aim to investigate the nature of the rock failure that can occur with increasing confining pressure, but the pore fluid system was not included in these experiments. Therefore, the fluid pressure and overpressure phenomena in actual geological settings are not considered in the experiment, although these factors play an important role in rock deformation.

2.3. Results

The average density of the sample is 2.45 g/cm^3. The X-ray diffraction results show that the minerals in the mudstone samples comprise clay (28.6%), quartz (29.6%), plagioclase (7.8%), calcite (11.8%), dolomite (12.9%), analcite (3.7%), anhydrite (1.2%) and iron dolomite (3.5%).

Based on the triaxial compression test, stress–strain curves of mudstone were obtained and the Young's modulus E, Poisson's ratio v, Bulk modulus K and Shear modulus G and Differential stress strength were calculated for different confining pressures (Table 1). The calculation methods for these mechanical parameters are as follows:

$$E = \frac{\Delta\sigma}{\Delta\varepsilon_1};\ v = \frac{\Delta\varepsilon_2}{\Delta\varepsilon_1};\ K = \frac{E}{3(1-2\nu)};\ G = \frac{E}{2(1+\nu)}$$

where $\Delta\sigma$ is the stress difference in the elastic deformation stage before the peak value, $\Delta\varepsilon_1$ is the axial strain difference corresponding to $\Delta\sigma$, and $\Delta\varepsilon_2$ is the radial strain difference corresponding to $\Delta\sigma$.

Table 1. Test results of rock mechanical parameters.

Sample Number	Confining Pressure [MPa]	Young Modulus [GPa]	Poisson Ratio	Differential Stress Strength [MPa]	Bulk Modulus [GPa]	Shear Modulus [GPa]
1#	0	3.56	0.23	28	2.2	1.45
2#	10	9.12	0.17	106.7	4.61	3.90
3#	20	11.76	0.16	125.3	5.76	5.07
4#	40	15.74	0.17	196.7	7.95	6.73

The mechanical parameters of mudstone vary significantly with increasing confining pressure. Young's modulus ranges between 3.56 GPa and 15.74 GPa, and Poisson's ratio ranges between 0.17 and 0.23. Due to the limited number of core samples, only one test was conducted under each confining pressure condition. To minimize experimental data distortion, a mathematical model of confining pressure and mechanical parameters was constructed using the least squares method. Figure 3 shows the variation of rock's elastic modulus with confining pressure, where the blue line and points represent the bulk modulus data, and the purple line and points denote the shear modulus data. From this figure, it can be observed that as confining pressure increases, both bulk modulus K (Equation (1)) and shear modulus G (Equation (2)) increase with an approximately linear relationship.

$$K = 0.1375\sigma_3 + 2.742\ (R^2 = 0.9597) \tag{1}$$

$$G = 0.125\sigma_3 + 2.0958\ (R^2 = 0.9266) \tag{2}$$

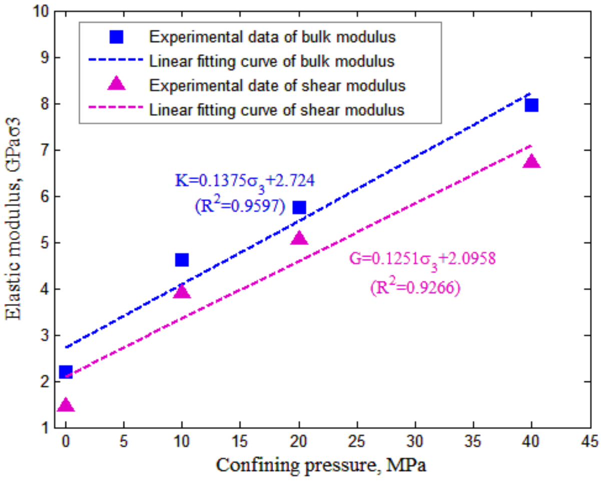

Figure 3. Variation of rock elastic modulus with confining pressure; blue line and point are data of bulk modulus, while purple line and point denote data of shear modulus.

This feature can be understood in terms of the lateral compaction effect of confining pressure on the rock sample causing the increase in rock strength. This means that as confining pressure increases, the rock's ability to resist elastic deformation (volume deformation or shear deformation) also increases. Therefore, the increase in confining pressure also enhances the rock's strength and elastic properties, consistent with observations in tests by other authors [31]. The mathematical model in Equations (1) and (2) establishes the basis for assigning mechanical parameters in the subsequent numerical experiments.

Based on the stress conditions (confining pressure, differential stress) applied to four rock samples, the Mohr–Coulomb failure envelope has been drawn, as shown in Figure 4. Using the modified Griffith criterion [24] (Equation (3)), the shear rupture parameters (cohesion, internal friction angle) of the rock have been calculated, as shown in Table 2.

$$\tau_s = \mu\sigma_n + 2T \tag{3}$$

where τ_s is the shear stress, σ_n is the normal stress; μ is the internal friction coefficient, φ is the internal friction angle; T is the tensile strength, and according to the Coulomb failure criterion, cohesion $c = 2T$.

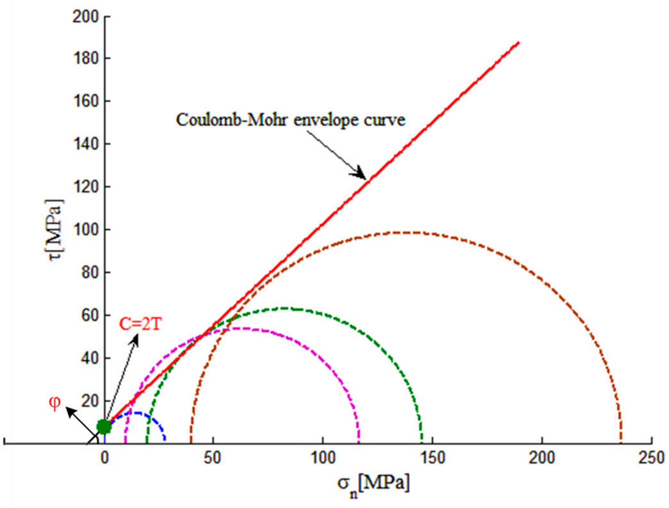

Figure 4. Stress Mohr–Coulomb failure envelope curve, represented by different colors for stress Mohr circles under different confining pressures, including blue: 0 MPa, purple: 10 MPa, green: 20 MPa, and brown: 40 MPa.

Table 2. Calculation results of rock shear parameters.

Confining Pressure [MPa]	Rock Strength [MPa]	Cohesion [MPa]	Internal Friction Angle [°]	Tensile Strength [MPa]
0	28	8.96	37.72	4.48
10	106.7			
20	125.3			
40	196.7			

The cohesion of rock reflects the degree of consolidation. In shallow buried conditions (low confining pressure condition), the degree of consolidation is low, and the cohesion is smaller. In deep buried conditions (high confining pressure condition), the degree of consolidation is high, and the cohesion is larger. However, for consolidated rock, it is generally believed that the deformation characteristics under low confining pressure adhere to the Coulomb fracture criterion, with little change in the cohesion and internal friction angle. However, with increasing temperature, pressure or water bubbling, the degree of consolidation changes, leading to a transition from brittle to ductile rock, causing alterations in the cohesion and internal friction angle [32]. The cohesion and internal friction angle obtained in our experiment are derived from Mohr–Coulomb fracture envelope under low confining pressure. For deformation under high confining pressure, the relationship between the change factor of cohesion and internal friction angle and plastic strain is modeled in the simulation process through numerical methods, as shown in Table 3, reflecting the variation in cohesion and internal friction angle with plastic strain during rock deformation.

Table 3. The relationship between cohesion change factor (W_c), friction angle change factor (W_φ) and plastic strain (ε^P).

ε^P (%)	W_c	W_φ
0	1	0
5	0.5	3.0
10	0.5	2.0
100	1	0

3. Numerical Simulation of Mechanical Deformation of Mudstone with High Confining Pressure

3.1. Deformation and Numerical Modelling Methodologies

The numerical code FLAC3D, a finite difference solver for engineering and rock mechanics problems [33], was used for the modeling conducted in this study. The code can continuously simulate the stress behavior and analyze the plastic flow of rock. The material in the model is divided into a large number of grids, and the actual structure is represented by adjusting polyhedral elements in the three-dimensional grid. Each grid unit is assigned material properties such as bulk modulus, shear modulus and density. Based on the principles of linear or nonlinear pressure or strain, each element can deform when subjected to external forces and boundary conditions. Since its solution is obtained through a numerical relaxation method without a matrix form, it allows for abundant three-dimensional computations with a small computational memory.

Based on the continuum form of the momentum principle, Cauchy's equation of motion can be obtained as [34]:

$$\frac{\partial \sigma_{ij}}{\partial x_j} + \rho g_i + c\dot{u} = \rho\left(\frac{\partial \dot{u}_i}{\partial t}\right) \tag{4}$$

where ρ is mass density, t is time, x_i are the components of coordinate vector, g_i are the components of gravitational acceleration, and σ_{ij} are the components of the stress tensor and $c\dot{u}$ is the damping term.

The acceleration is zero in the case of static equilibrium:

$$c\dot{u} \Rightarrow \rho(\frac{\partial \dot{u}_i}{\partial t}) \tag{5}$$

The equation of equilibrium can be rewritten as:

$$\frac{\partial \sigma_{ij}}{\partial x_j} + \rho g_i = 0 \tag{6}$$

The strain rate $\dot{\varepsilon}_{ij}$ is derived from velocity gradient as:

$$\dot{\varepsilon}_{ij} = \frac{1}{2}(\frac{\partial \dot{u}_i}{\partial x_j} + \frac{\partial \dot{u}_j}{\partial x_i}) \tag{7}$$

The mechanical deformation of the model is governed by the Strain-Softening Mohr–Coulomb Model, which involves constitutive parameters including shear modulus (G), bulk modulus (K), cohesion (C), tensile strength (T) and friction angle (j). Under mechanical loading, the Mohr–Coulomb yielding criteria can be described by

$$|\tau_s| = C + \sigma_n \tan \varphi \tag{8}$$

where C is the cohesion, φ is the angle of friction, and σ_n and τ are the normal and shear stress, respectively, acting on a plane.

In order to reflect the strain softening characteristics in the peak–post failure behavior, softening parameters are defined in advance according to the principle of piecewise linearity. After the plastic strain is generated, part or all of the shear parameters, including the cohesion, internal friction angle and tensile strength, will change.

For each cell, two softening parameters, Δk^s and Δk^t, are, respectively, defined as the plastic softening increment and the tensile softening increment. The shear and tensile softening modulus in the basic tetrahedral elements can be calculated using the code FLAC3D. For a specified tetrahedron, the shear softening increment is defined by the second invariant of the plastic shear strain increment tensor, namely [33]:

$$\Delta k^s = \sqrt{[(\Delta\varepsilon_1^{ps} - \Delta\varepsilon_m^{ps})^2 + (\Delta\varepsilon_m^{ps})^2 + (\Delta\varepsilon_3^{ps} - \Delta\varepsilon_m^{ps})^2]/2} \tag{9}$$

where $\Delta\varepsilon_m^{ps}$ is the bulk plastic shear strain modulus, $\Delta\varepsilon_m^{ps} = \left(\Delta\varepsilon_1^{ps} + \varepsilon_3^{ps}\right)/3$; $\Delta\varepsilon_1^{ps}$ and $\Delta\varepsilon_3^{ps}$ are plastic shear strain increment in the first and third principal stress directions.

The tensile softening increment is expressed by plastic tensile strain increment $\Delta\varepsilon_3^{pt}$ as

$$\Delta \mathrm{k}^{\mathrm{t}} = \left|\Delta\varepsilon_3^{pt}\right| = \left|\frac{\sigma_3^I - \sigma^t}{\alpha_1}\right| \tag{10}$$

where σ_3^I is the trial stress in the iterative process, and α_1 is the material constant defined by the shear modulus.

When the plastic deformation occurs, the cohesion C_p and internal friction angle φ_p are defined as follows:

$$\mathrm{C_p} = \mathrm{W_c C} \tag{11}$$

$$\varphi_{\mathrm{p}} = \varphi - \mathrm{W}_{\varphi} \tag{12}$$

where *C* is the initial cohesion, φ denotes internal friction angle, W_c and W_φ are the change factors of cohesion and internal friction angle, respectively, which are related to the plastic strain ε^p, as shown in Table 3 [35,36].

Based on FLAC3D, large-scale numerical models (Figure 5a) for physical experimental rock samples are constructed. The wall softening Mohr–Coulomb model is adopted, and the relevant mechanical and shear parameters are assigned. A constant stress boundary (confining pressure condition) is applied along the X direction, and then a load is applied at a certain rate (m/step) along the Y direction (Figure 5b). The displacement of the grid point (0,0,0) moving in the Y direction and the stress of the element in the Y direction are recorded until the stress reaches its peak and starts to fall, thereby capturing the full stress–strain deformation characteristics. Finally, the strain distribution and deformation mode of the rock sample are analyzed on the FLAC3D platform (Figure 5c). For rock samples subjected to numerical simulation tests, different colors are used to indicate varying degrees of strain, with blue indicating a lower degree of strain and red indicating a higher degree of strain. Areas with concentrated and high strain are more prone to fracture.

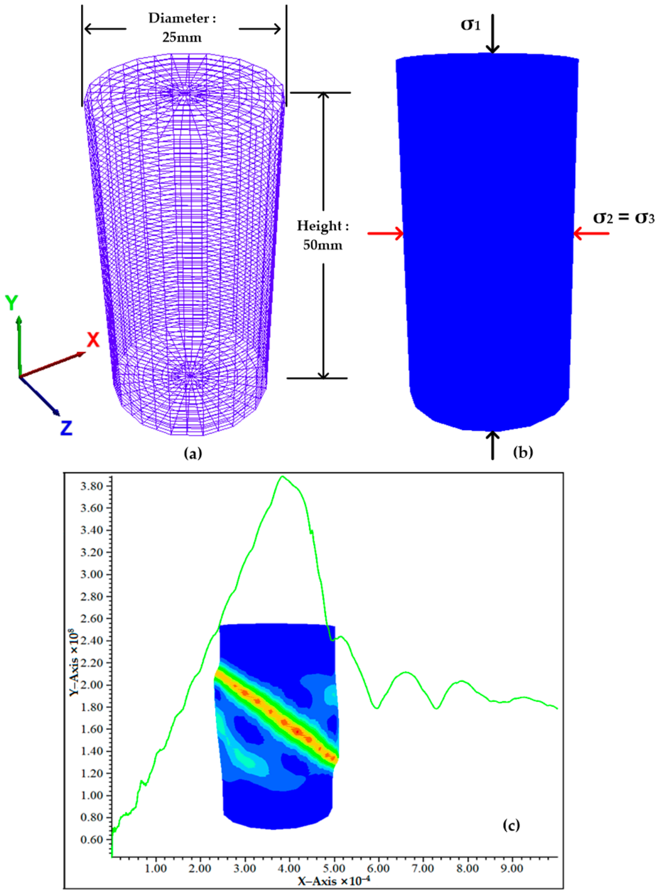

Figure 5. Numerical modeling and simulation process. (**a**) Large-scale numerical models, (**b**) loading direction of stress, (**c**) the stress and deformation curves, as well as the deformation characteristics of the rock sample, where colors represent the strain distribution pattern, and the areas where strain is concentrated are the parts of the rock sample that are prone to developing cracks (such as the red distribution area).

3.2. Numerical Modelling Results

(1) Numerical Model Calibration by Comparison between Numerical Results and Experimental Tests

Cylindrical numerical models with a diameter of 25 mm and a height of 50 mm are constructed to represent mudstone specimens in the triaxial loading test. Based on the mechanical parameters (Table 1) and shear parameters (Table 2) under different confining pressure conditions, the values of these mechanical parameters are assigned to the numerical model. The same confining pressure condition as in the physical experiment is applied using the FLAC3D. Rock sample deformation data, including the displacements of grid points and stresses of zones, are collected during the loading process. When the stress decreases from the peak value to the residual stress intensity, loading is stopped. The regions where the strain is concentrated in the rock sample correspond to the rock failure zones. A stress–strain curve and rock failure behaviors for different confining pressures can then be obtained. The size of the three-dimensional grid and the axial loading rate are adjusted in FLAC3D until the mechanical properties calculated by FLAC3D match those obtained in the laboratory. Finally, the numerical model (16,384 grid cells and 16,705 grid nodes) is finalized with a rate of 1×10^{-7} m/step. Figure 6 presents a comparison between the numerical and physical test results. From this figure, it is observed that the rock forms nearly axial splitting under the condition of no confining pressure. With the increase in confining pressures, a single shear fracture develops, and conjugate shear fractures appear at a confining pressure of 40 MPa. The strain distribution characteristics obtained by numerical simulation are consistent with the failure modes observed in the laboratory experiments. In Figure 6a, the simulation diagram of 0 confining pressure condition differs slightly from the experimental results, because the four rock samples cannot be fully sampled in parallel. The cohesion and internal friction angle are obtained based on the mechanical data of the four cores, which may introduce some differences between the simulation and the experimental results, but the simulated fracture mode remains similar. In Figure 6b, the solid green lines represent the experimental test results, while the dotted blue lines represent the numerical simulation results. The overall shape and peak strain match between the experimental and numerical results, although the two curves show basically no overlap. Overall, the numerical model captures the stress–strain behavior and failure modes demonstrated by the laboratory experiments. In future studies, this numerical model will be used to investigate mudstone failure behavior at different confining pressures and evaluate the brittle–ductile failure characteristics.

(2) Mechanical Failure Behavior of Mudstone under High Confining Pressure

To obtain the evolution process of rock failure behavior with the increasing confining pressures, the confining pressures adopted in the numerical experiment are 15 MPa, 30 MPa, 45 MPa, 60 MPa, 75 MPa, 90 MPa, 105 MPa, 120 MPa, 135 MPa and 150 MPa. The mechanical deformation characteristics and stress–strain curves of mudstone under different confining pressures are shown in Figure 7. Figure 7 displays the different failure modes the rock experiences with increased confining pressure: high-angle shear fracture and high-angle conjugate shear fracture for low confining pressures, and low-angle shear fracture and low-angle conjugate shear fracture for high confining pressures. For the confining pressure less than 30 MPa, a single high-angle shear fracture predominantly forms with a peak strain of less than 3%. When the confining pressure is between 30 MPa and 60 MPa, the rock sample mainly develops high-angle conjugate shear fractures with a peak strain of 3~5%. When the confining pressure is 60–105 MPa, the low-angle shear fracture is mainly developed with peak strain of 5–7%. When the confining pressure is greater than 105 MPa, low-angle conjugate shear fractures mainly develop with peak strain greater than 7%.

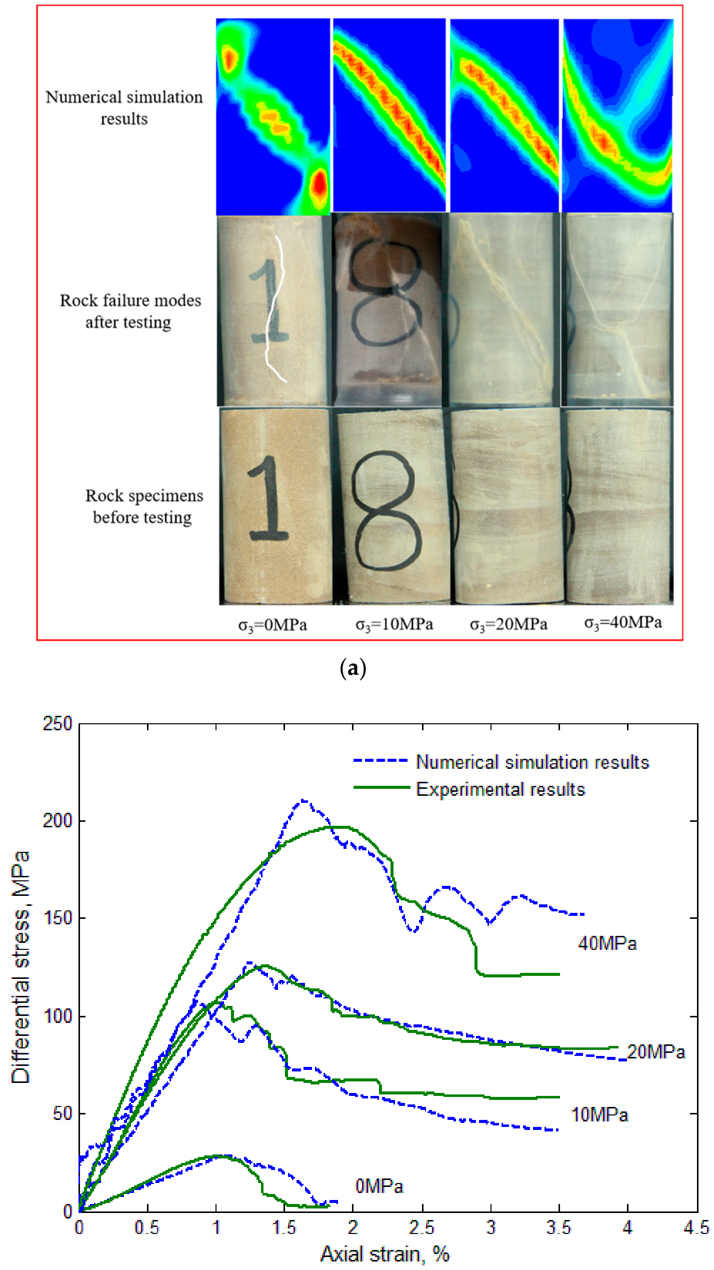

(**a**)

(**b**)

Figure 6. Comparison between numerical results and physical testing results. (**a**) Rock failure modes, where colors represent the strain distribution pattern, and the areas where strain is concentrated are the parts of the rock sample that are prone to developing cracks (such as the red distribution area), (**b**) stress–strain curve characteristic.

At high confining pressures, the numerical results are not compared with the laboratory experimental results, and there is a lack of data to demonstrate the reliability of the model. However, the mudstone still exhibits failure behavior at high confining pressures, and the fracture angle decreases as confining pressure increases, which is consistent with observations in tests by other authors [13,37]. For instance, Iyare et al. [13] observed that mudstone can still undergo brittle or brittle–ductile failure transition with a significant stress drop at confining pressure up to 130 MPa in a triaxial loading experiment.

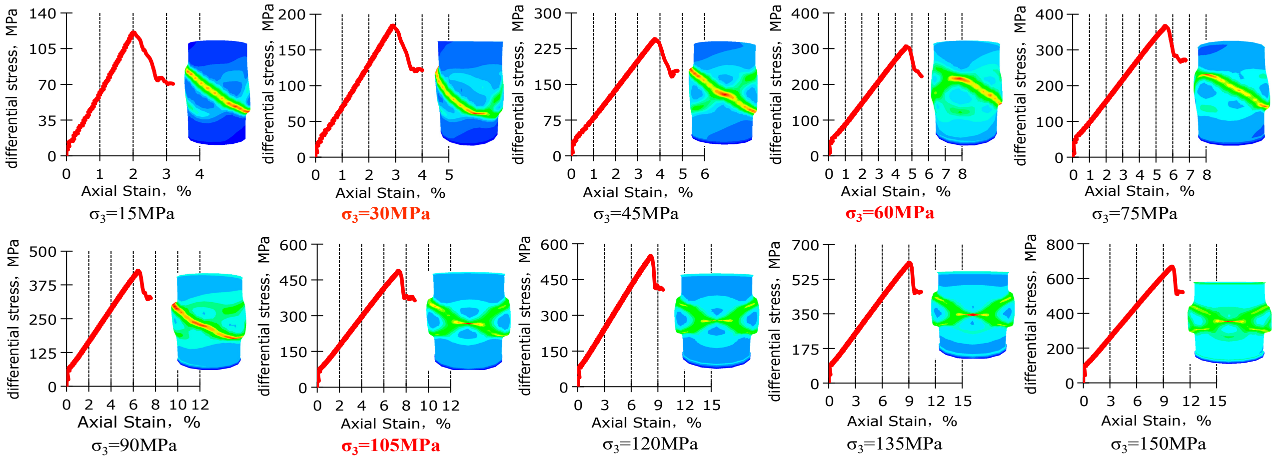

Figure 7. Mudstone failure characteristics with confining pressure, where the confining pressure marked by the red font is the critical state for the transition of the failure modes. The colors in the rock sample represent the strain distribution pattern, and the areas where strain is concentrated are the parts of the rock sample that are prone to developing cracks (such as the red distribution area).

4. Discussions

4.1. Mudstone Failure Mechanism with Increasing Confining Pressure

Confining pressure and differential stress (or deviator stress) are the main mechanical conditions affecting rock fracture behavior. The confining pressure acts as a compaction on the rock and inhibits the rock from undergoing shear fracture, while differential stress (or deviator stress) promotes shear fracture and forms a slip fault. Generally, rock deformation transitions from brittle to ductile behavior as confining pressure increases.

In this paper, we focus on the failure mechanism of mudstone under increasing confining pressure through numerical experiments, adopting the Strain-Softening Mohr–Coulomb Model provided by FLAC3D, in which ductile flow is not included. The rock deformation transitions from shear-enhanced dilatancy (brittle failure) to shear-enhanced compaction (brittle–ductile transition failure). At the low confining pressures, shear-enhanced dilatancy behavior occurs in rock under the shear stress τ (differential stress), while at the high confining pressures, shear-enhanced compaction behavior is observed in rock deformation.

(1) Failure Mechanism At Low Confining Pressures

In order to better understand the failure mechanism, we assume an ideal microscopic model that only considers the mechanical deformation process of two particles in the rock, where particle B is fixed and particle A can move under the applied force. At low confining pressures, shear stress (differential stress) is the main stress condition controlling rock fracture, while confining pressure has little effect on rock deformation. Therefore, the distance between particles A and B increases due to shear stress, which eventually leads to the bond breaking between the two particles and the shear-enhanced dilatancy in the rock (Figure 8a).

Prior to the breaking of the bond between A and B, particle A is subjected to three forces: the shear stress τ, the static friction force f exerted by the surrounding rock and the stress c exerted by particle B (c is considered as the cohesion force of the rock). The stress direction is shown in Figure 8a. Critical mechanical conditions for rock failure are as follows:

$$\tau = c + f_{\max} \tag{13}$$

Moreover,

$$f_{\max} = \sigma \tan \varphi = \sigma \mu$$

In Equation (13), cohesion c represents the indirect contact stress between two adjacent particles in the rock [18]. $f_{\max}$ is the maximum static friction stress, which prevents the particles from moving relative to each other; its direction is opposite to the movement trend of the particles. φ is the angle of internal friction, μ is the coefficient of internal friction, and σ is the normal stress. Equation (13) is the Coulomb failure criterion, which is only applicable to describe rock shear dilatancy fracture at low confining pressure.

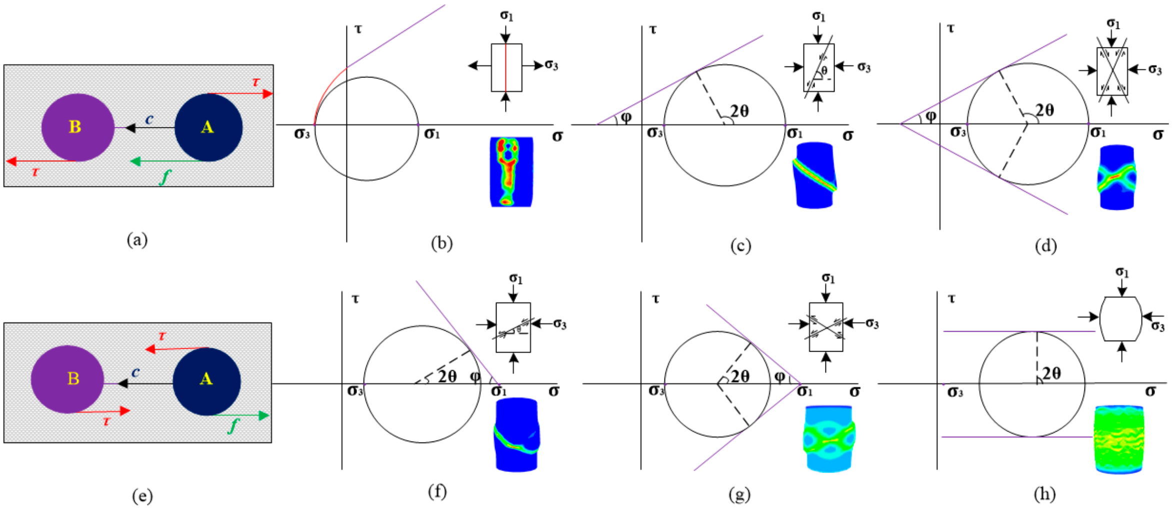

Figure 8. The transition of failure modes with increasing confining pressure. At low confining pressure (**a**–**d**): ideal stress model of rock (**a**), the deformation mechanism of high-angle splitting fracture (**b**), high-angle shear fracture (**c**) and high-angle conjugate shear fracture (**d**); at high confining pressure (**e**–**h**): ideal stress model of rock (**e**), the deformation mechanism of low-angle shear fracture (**f**), low-angle conjugate shear fracture (**g**) and plastic deformation (**h**). The colors in the rock sample represent the strain distribution pattern, and the areas where strain is concentrated are the parts of the rock sample that are prone to developing cracks (such as the red distribution area).

In the loading process, when the differential stress $|\sigma_1 - \sigma_3| = \sigma_0$ (σ_0 is differential stress strength of rock failure), the rock starts to fail. It is worth noting that when $\sigma_3 > 0$, the article mainly discusses the shear fracture caused by rock compression. However, when $\sigma_3 < 0$, the rock fracture criterion meets the Griffith criterion [24]. When $\sigma_3 \leq -\sigma_t$, the rock sample undergoes tensile fracture, mainly forming a large-angle splitting fracture of about 90° (Figure 8b), with a fracture mode similar to uniaxial compression. When σ_3 is small enough to satisfy $0 < \sigma_3 < \sigma_0$, a single shear fracture with a high angle is formed at only axial stress loading to $\sigma_1 = \sigma_0 + \sigma_3$, which reaches the tangent of Mohr circle and Coulomb failure envelope curve (Figure 8c). The shear fracture angle θ can be estimated using Mohr's circle and the damage envelope. The angle that is measured from the center of the circle in an anticlockwise direction between the normal stress axis and the failure point is equal to twice the shear fracture angle (2θ) [13]. The shear fracture angle is expressed by Equation (14).

$$\theta = 45^\circ + \frac{\varphi}{2} \tag{14}$$

When the confining pressure increases to $\sigma_3 > \sigma_0$ (but σ_3 still belongs to low confining pressure field), rock failure occurs at $\sigma_1 = \sigma_3 - \sigma_0$ and $\sigma_1 = \sigma_0 + \sigma_3$, resulting in the development of high-angle conjugate shear fractures with the increasing axial pressure σ_1 (Figure 8d).

(2) Failure Mechanism At High Confining Pressures

For deep burial, confining pressure becomes the main stress condition controlling rock fracture, so compaction plays a leading role under high confining pressure. As a result, the shear-enhanced compaction effect appears under low shear stress [23], promoting a relative decrease in the distance between two particles due to the compaction effect. Therefore, the direction of internal friction stress f applied by particle A is opposite to the direction of cohesion c (Figure 8e) and the Coulomb fracture criterion (Equation (13)) is not suitable for this case. The critical condition for rock failure is when the shear stress is equal to the difference between internal friction stress and cohesion stress:

$$\tau = c - \sigma \tan \varphi \tag{15}$$

At this time, the slope of the failure envelope in curve Equation (15) becomes negative. When the Mohr circle is tangent to the failure envelope curve, rock fails. A shear fracture angle θ is given by Equation (16):

$$\theta = 45^\circ - \frac{\varphi}{2} \tag{16}$$

Therefore, it is easy to form low-angle shear fracture under the high confining pressure (Figure 8f). Similarly, the rock finally develops low-angle conjugate shear fractures under increased confining pressures (Figure 8g). When the confining pressure becomes excessively high, the rock sample undergoes primarily plastic deformation, with the internal friction angle approaching zero, and no distinct fracture (Figure 8h).

4.2. A New Model to Predict Brittle–Ductile Failure Behavior of Mudstone

Based on the analysis of the mudstone failure mechanism, the rock fracture modes under low and high confining pressure are defined, respectively, which helps to better understand mudstone failure behavior as confining pressure increases. A new model is proposed to predict rock failure behavior. Figure 9 compares the conventional failure model with the new failure model proposed in this study. The new model exhibits failure modes the rock undergoes at failure with the confining pressure: high-angle single shear fractures, high-angle conjugate shear fractures, low-angle single shear fractures, low-angle conjugate shear fracture and ductile flow. Although ductile flow is not observed in this study, it may appear in rock deformation at high confining pressures [13,18]. At present, conventional models of failure behavior have been proposed in which failure modes the rock experiences at failure are shown as high-angle single shear fractures (axial splitting and shear fracture for brittle failure), conjugate shear fractures (shear band for brittle–ductile transition failure), and ductile flow (ductile failure) [18,38]. From this figure, brittle failure is mainly characterized by a rapid stress drop in the stress–strain curve. In the conventional failure model, failure modes mainly develop split or shear fractures at brittle failure, while in the new failure model, the development of the shear dilatancy fractures is defined as the main brittle failure behavior, and the failure modes mainly develop high-angle shear fractures (fracture angle $\theta > 45^\circ$) or high-angle conjugate shear fractures. At the brittle–ductile transition failure fields with a gradual stress drop, the new model explains shear compaction fractures as the behavior of brittle–ductile transition failure, with low-angle shear fractures (fracture angle $\theta < 45^\circ$) or low-angle shear conjugate fractures, while the shear conjugate fractures are generally regarded as a typical characteristic of brittle–ductile transition failure in the conventional model. Comparing the critical confining pressures at the beginning of the brittle–ductile transition in both the conventional model and new model, the new model predicts a higher value. Therefore, the new model provides a better understanding of fracture modes as confining pressure increases, which is very important for many engineering applications. For example, in geological engineering, the differences in fracture modes as predicted by the new model can aid in dividing rock mechanics layers. In hydraulic fracturing operations, it is preferable to induce shear dilatancy fractures rather than shear compaction fractures, as the former creates favorable channels for oil and gas.

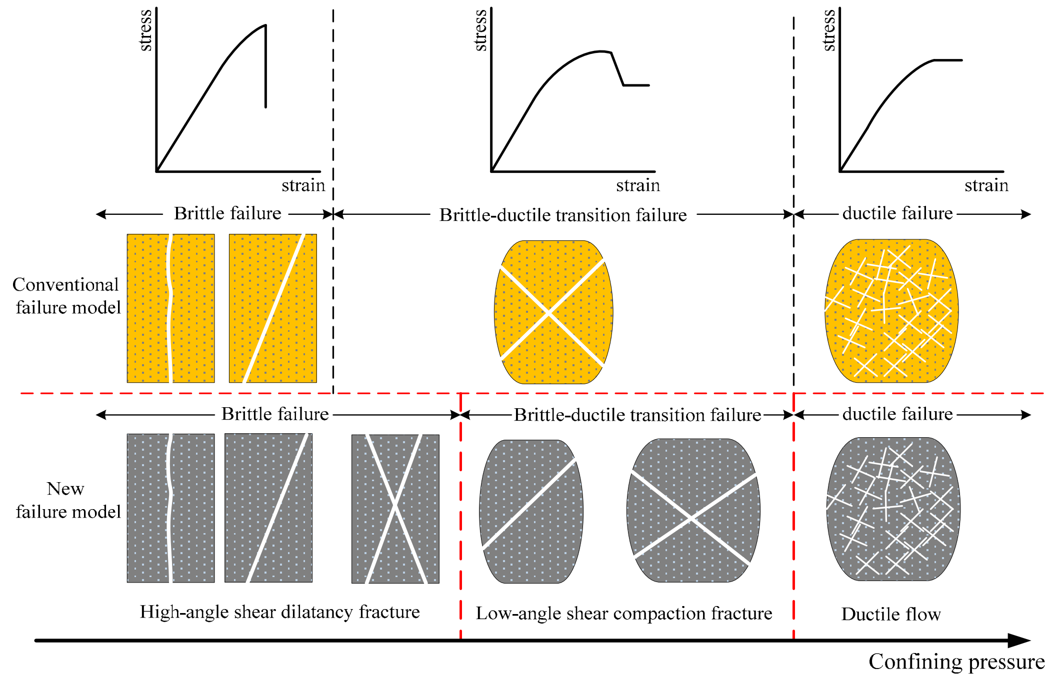

Figure 9. Comparison of the conventional failure model with the new failure model proposed in our studies.

4.3. Predicting the Brittle–Ductile Failure Behavior of Mudstone from the Kuqa Depression with Increasing Confining Pressure Based on the New Model

The new model is a physical model for qualitative description of brittle–ductile transition of rocks, without specific quantitative boundaries. In practice, the rock fracture mode is obtained through the mechanical deformation experiments. According to the new model, the critical condition for the brittle–ductile transition of rock is defined. Figure 10 depicts the evolution model of peak strain and failure modes with increasing confining pressure. From this figure, the rock peak strain shows a nearly linear change rule with the increasing confining pressure. At low confining pressure fields ($\sigma_3 < 60$ MPa), rock deformation mainly develops a high-angle shear dilatancy fracture with a peak strain less than 5%, showing obvious brittle failure. For confining pressure $\sigma_3 < 30$ MPa, a high-angle shear fracture is developed in the strain concentrated area with the peak strain less than 3%. When the confining pressure is between 30 MPa and 60 MPa, a high-angle conjugate shear fracture is developed with peak stain of 3~5%. At high confining pressure fields ($\sigma_3 > 60$ MPa), a high-angle shear compaction fracture is developed with a peak strain above 5%, exhibiting brittle–ductile transition failure. For the confining pressure σ_3 between 60 MPa and 105 MPa, the failure mode is characterized by low-angle single shear fractures with a peak strain of 5–7%, while for the confining pressure $\sigma_3 > 105$ MPa, a low-angle conjugate shear fracture appears in rock deformation with a peak strain of above 7%. In the new model, the critical confining pressure values at the beginning of the brittle–ductile transition are predicted to be $\sigma_3 = 60$ MPa, while this critical value predicted in the conventional model by Iyare et al. [13] is approximately 50 MPa from laboratory experiments. The result aligns with the conclusions mentioned in the new model, which is that the critical value predicted by the new model is greater than that of the conventional model.

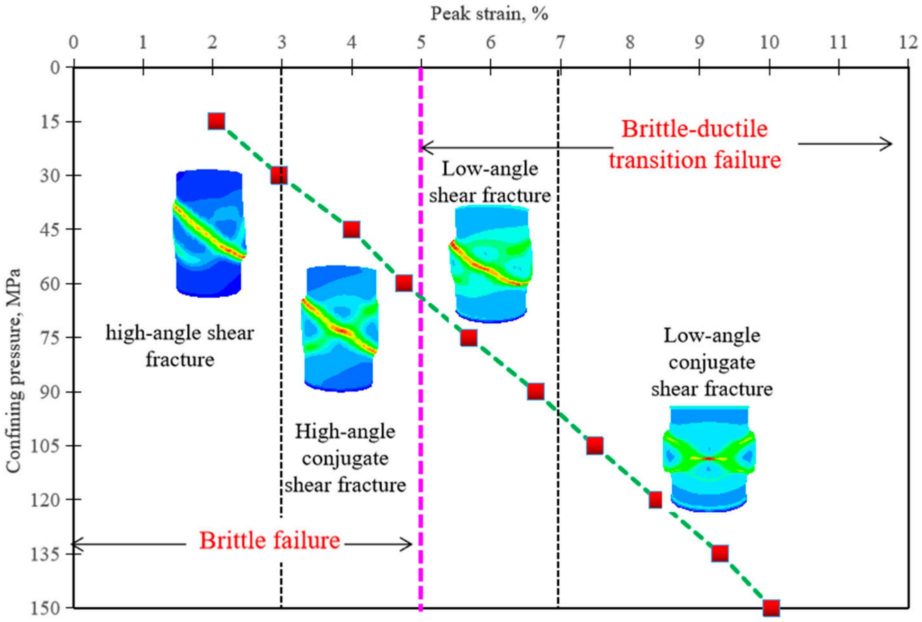

Figure 10. Evolution law of rock failure modes and peak strain with increasing confining pressure. The colors in the rock sample represent the strain distribution pattern, and the areas where strain is concentrated are the parts of the rock sample that are prone to developing cracks (such as the red distribution area).

5. Conclusions

(1) Laboratory experiments and numerical modeling are performed to study the mudstone caprocks from the Dongqiu Anticline of the Kuqa Depression in northern China. Based on the code FLAC3D, by adjusting the numerical model grid number and loading rate in the numerical experiments, the numerical model captures the stress–strain behavior and failure modes demonstrated by the laboratory experiments, and a reasonable numerical model is constructed for the mudstone specimen.

(2) A new model to predict brittle–ductile failure behavior of rocks is proposed by exploring the failure mechanism of mudstone under varying confining pressures. At low confining pressure, a shear dilatancy fracture appears in rock deformation, and the failure modes mainly develop high-angle shear fractures (fracture angle $\theta > 45°$) or high-angle conjugate shear fractures, exhibiting obvious brittle failure. At high confining pressures, a shear compaction fracture develops, and the fracture modes are shown as low-angle shear fractures (fracture angle $\theta < 45°$) or low-angle conjugate shear fractures, which are regarded as brittle–ductile transition failure behavior. In the ductile failure region, cataclastic or ductile flow occurs. The critical confining pressure values at the beginning of the brittle–ductile transition predicted by the new model are greater than those predicted by the conventional model. However, the new model provides a better understanding of the failure behavior as confining pressure increases.

(3) Based on the new model, the brittle–ductile failure behavior of mudstone from the Kuqa Depression is predicted with increasing confining pressure. The brittle failure mainly occurs at confining pressure less than 60 MPa with peak strain less than 5%. The brittle–ductile transition failure is exhibited in rock deformation at confining pressure greater than 60 MPa with peak strain greater than 5%.

Author Contributions: Conceptualization and methodology, X.F. and X.L.; investigation, Z.S. and K.X.; data curation, W.Z. and S.W.; writing—original draft, S.W.; writing—review and editing, W.Z. and K.X. All authors have read and agreed to the published version of the manuscript.

Funding: This research was supported by the Central Support Fund for the Reform and Development of Local Universities of China (2023JCYJ-02), the National Natural Science Foundation of China (52074088, 52474036, 52174022) and Key Project of the Joint Fund of Heilongjiang Provincial Natural Science Foundation of China (ZL2024E008).

Data Availability Statement: Data supporting the results of the research experiments can be obtained by contacting the corresponding author.

Conflicts of Interest: The author Xuesong Lu was employed by Research Institute of Petroleum Exploration and Development. The remaining authors declare that the research was conducted in the absence of any commercial or financial relationships that could be construed as a potential conflict of interest.

References

1. Wang, T.T.; Zhang, T.; Ranjith, P.G.; Li, Y.W.; Song, Z.L.; Wang, S.; Zhao, W.C. A new approach to the evaluation of rock mass rupture and brittleness under triaxial stress condition. *J. Pet. Sci. Eng.* **2020**, *184*, 106482. [CrossRef]
2. Gui, J.; Guo, J.; Sang, Y.; Chen, Y.; Ma, T.; Ranjith, P.G. Evaluation on the anisotropic brittleness index of shale rock using geophysical logging. *Petroleum* **2023**, *9*, 545–557. [CrossRef]
3. Xu, W.; Qu, X.; Yan, L.; Ning, Y. Experimental Study on Mechanical Properties and Permeability Characteristics of Calcareous Mudstone under Different Confining Pressures. *Materials* **2024**, *17*, 2731. [CrossRef] [PubMed]
4. Liu, S.-L.; Zhu, Q.-Z.; Zhao, L.-Y.; Yu, Q.-J.; Zhang, J.; Cao, Y.-J. Experimental investigation and micromechanics-based constitutive modeling of the transition from brittle to ductile behavior in saturated low-porosity rocks. *Appl. Math. Model.* **2024**, *126*, 506–525. [CrossRef]
5. Zhang, G.; Wu, S.; Guo, P.; Zhang, S. Mechanical Deformation, Acoustic Emission Characteristics, and Microcrack Development in Porous Sandstone During the Brittle–Ductile Transition. *Rock Mech. Rock Eng.* **2023**, *56*, 9099–9120. [CrossRef]
6. Rutter, E.H.; Glover, C.T. The deformation of porous sandstones; are Byerlee friction and the critical state line equivalent. *J. Struct. Geol.* **2012**, *44*, 129–140. [CrossRef]
7. Li, Q.; Cheng, Y.; Li, Q.; Zhang, C.; Ansari, U.; Song, B. Establishment and evaluation of strength criterion for clayey silt hydrate-bearing sediments. *Energy Sources Part A Recovery Util. Environ. Eff.* **2018**, *40*, 742–750. [CrossRef]
8. He, M.; Zuo, J.; Yuan, Z.; Ma, X.; Zhang, Z.; Ma, C. Criterion for residual strength and brittle-ductile transition of brittle rock under triaxial stress conditions. *Geoenergy Sci. Eng.* **2024**, *243*, 213340. [CrossRef]
9. Shen, Y.; Yuan, J.; Hou, X.; Hao, J.; Bai, Z. The strength changes and failure modes of high-temperature granite subjected to cooling shocks. *Geomech. Geophys. Geo-Energy Geo-Resour.* **2021**, *7*, 23. [CrossRef]
10. Sitzia, F.; Pires, V.; Lisci, C. Exploring the Mechanical Properties of Stone Heritage: Investigating the Effects of Low Temperatures on Ductile—Brittle Transition. *Geoheritage* **2023**, *15*, 123. [CrossRef]
11. Qiu, G.; Chang, X.; Li, J.; Guo, Y.; Wang, L.; Ma, H.; Guo, W.; Bi, Z. Study on rock brittleness characteristics of deep volcanic reservoir under different confining pressures. *J. Pet. Explor. Prod. Technol.* **2023**, *14*, 453–476. [CrossRef]
12. Wang, J.; Du, J.; Li, W.; Chen, X.; Zhang, H.; Wang, T.; Li, Z.; Hao, R. Brittleness index evaluation of gas-bearing sandstone under triaxial compression conditions. *Geomech. Geophys. Geo-Energy Geo-Resour.* **2023**, *9*, 160. [CrossRef]
13. Iyare, U.C.; Blake, O.O.; Ramsook, R. Modelling the Failure Behaviour of Mudstones under High Pressures. *Rock Mech. Rock Eng.* **2021**, *54*, 2815–2828. [CrossRef]
14. Lei, W.; Liu, X.; Ding, Y.; Xiong, J.; Liang, L. The investigation on shale mechanical characteristics and brittleness evaluation. *Sci. Rep.* **2023**, *13*, 22936. [CrossRef]
15. Wang, H.; Wu, T.; Fu, X.; Liu, B.; Wang, S.; Jia, R. Quantitative determination of the brittle–ductile transition characteristics of caprocks and its geological significance in the kuqa depression, tarim basin, western China. *J. Pet. Sci. Eng.* **2019**, *173*, 492–500. [CrossRef]
16. Paterson, M.S.; Wong, T.F. *Experimental Rock Deformation—The Brittle Field*, 2nd ed.; Spinger: New York, NY, USA, 2005.
17. Engelder, T.; Behr, R.A. Skempton's poroelastic relaxation: The mechanism that accounts for the distribution of pore pressure and exhumation-related fractures in black shale of the appalachian basin. *AAPG Bull.* **2021**, *105*, 669–694. [CrossRef]
18. Wang, S.; Zhao, W.; Fu, X.; Zhang, Z.; Wang, T.; Ge, J. A universal method for quantitatively evaluating rock brittle-ductile transition behaviors. *J. Pet. Sci. Eng.* **2020**, *195*, 107774. [CrossRef]

19. Zhao, G.; Guo, Y.; Yang, C.; Wang, L.; Guo, W.; Yang, H.; Wu, X.; Liu, H. Anisotropic mechanical behavior of ultra-deep shale under high in-situ stress, a case study in the Luzhou block of the southern Sichuan Basin, China. *Int. J. Rock Mech. Min. Sci.* **2023**, *170*, 105536. [CrossRef]
20. Herrmann, J.; Rybacki, E.; Sone, H.; Dresen, G. Deformation experiments on bowland and posidonia shale—Part i: Strength and young's modulus at ambient and in situ pc-T conditions. *Rock Mech. Rock Eng.* **2018**, *51*, 3645–3666. [CrossRef]
21. Evans, B.; Fredrich, J.T.; Wong, T.-F. The Brittle-Ductile Transition in Rocks: Recent Experimental and Theoretical Progress. In *The Brittle-Ductile Transition in Rocks*; American Geophysical Union (AGU): Washington, DC, USA, 2013.
22. Chelidze, T.; Matcharashvili, T.; Abashidze, V.; Tsaguria, T.; Dovgal, N.; Zhukova, N. Complex dynamics of fault zone deformation under large dam at various time scales. *Geomech. Geophys. Geo-Energy Geo-Resour.* **2019**, *5*, 437–455. [CrossRef]
23. Fossen, H.; Schultz, R.A.; Shipton, Z.K.; Mair, K. Deformation bands in sandstone: A review. *J. Geol. Soc.* **2007**, *164*, 755–769. [CrossRef]
24. Griffith, A.A. The phenomena of rupture and flow in solids. *Philos. Trans. R. Soc. Lond.* **1920**, *A221*, 163–198.
25. Li, H.; Pel, L.; You, Z.; Smeulders, D. Stress-dependent instantaneous cohesion and friction angle for the Mohr–Coulomb criterion. *Int. J. Mech. Sci.* **2024**, *283*, 109652. [CrossRef]
26. Wang, T.; Liu, Y.; Cai, M.; Zhao, W.; Ranjith, P.G.; Liu, M. Optimization of rock failure criteria under different fault mechanisms and borehole trajectories. *Geomech. Geophys. Geo-Energy Geo-Resour.* **2022**, *8*, 127. [CrossRef]
27. De Paola, N.; Faulkner, D.R.; Collettini, C. Brittle versus ductile deformation as the main control on the transport properties of low-porosity anhydrite rocks. *J. Geophys. Res. Solid Earth* **2009**, *114*, 1–17. [CrossRef]
28. Fu, X.F.; Song, Y.; Lv, Y.F.; Sun, Y.H. Rock mechanic characteristics of gysum cover and conservation function to gas in the Kuqa depression, the Tarim basin. *Pet. Geol. Exp.* **2006**, *28*, 25–29.
29. Eberl, D.D. *User's Guide to RockJock—A Program for Determining Quantitative Mineralogy from Powder X-Ray Diffraction Data*; U.S. Geological Survey Open-File Report 03-78; USGS: Reston, VA, USA, 2003; pp. 40–42.
30. Liu, G.; Shang, D.; Zhao, Y.; Du, X. Characterization of brittleness index of gas shale and its influence on favorable block exploitation in southwest China. *Front. Earth Sci.* **2024**, *12*, 1389378. [CrossRef]
31. Shi, L.; Zeng, Z.; Fang, Z.; Li, X. Investigation of the effect of confining pressure on the mechanics-permeability behavior of mudstone under triaxial compression. *Geofluids* **2019**, *219*, 1–14. [CrossRef]
32. Itasca. *Fast Lagrangian Analysis of Continua in 3 Dimensions, User Manual*, version 3.1; Itasca Consulting Group, Inc.: Minneapolis, MN, USA, 2005.
33. Li, Q.; Liu, L.; Yu, B.; Guo, L.; Shi, S.; Miao, L. Borehole enlargement rate as a measure of borehole instability in hydrate reservoir and its relationship with drilling mud density. *J. Pet. Explor. Prod.* **2021**, *11*, 1185–1198. [CrossRef]
34. Strayer, L.M.; Hudleston, P.J.; Lorig, L.J. A numerical model of deformation and fluid-flow in an evolving thrust wedge. *Tectonophysics* **2001**, *335*, 121–145. [CrossRef]
35. He, Z.M.; Lin, H.; Zhou, L.J. The Numerical Modelling for the Stress Characteristic of Stratified Rock Samples under Uniaxial Compression. In Proceedings of the Geohunan International Conference, Changsha, China, 9–11 June 2011.
36. Hwang, R.H.; Yang, T.H.; Yu, Q.L. Numerical Simulation of Effect of Fracture Distribution on Failure Mechanism of Tunnel. *Adv. Mater. Res.* **2012**, *446–449*, 652–656. [CrossRef]
37. Zhang, H.; Li, C.C. Effects of confining stress on the post-peak behaviour and fracture angle of fauske marble and iddeford granite. *Rock Mech. Rock Eng.* **2019**, *52*, 1377–1385. [CrossRef]
38. Cheng, G.; Jiang, B.; Li, F.; Li, M.; Song, Y.; Hou, C. Experimental study on brittle-to-ductile transition mechanism of lower Silurian organic-rich shale in south China. *Int. J. Rock Mech. Min. Sci.* **2023**, *170*, 105543. [CrossRef]